

Magnetic Anisotropy Induced by Orbital Occupation States in $\text{La}_{0.67}\text{Sr}_{0.33}\text{MnO}_3$ Film

Huaixiang Wang

Chinese Academy of Sciences Institute of Physics

Jinghua Song

Chinese Academy of Sciences Institute of Physics

Weipeng Wang

Chinese Academy of Sciences Institute of Physics

Yuansha Chen

Chinese Academy of Sciences Institute of Physics

Xi Shen

Chinese Academy of Sciences Institute of Physics

Yuan Yao

Chinese Academy of Sciences Institute of Physics

Junjie Li

Chinese Academy of Sciences Institute of Physics

Jirong Sun

Chinese Academy of Sciences Institute of Physics

R.C. Yu (✉ rcyu@iphy.ac.cn)

Chinese Academy of Sciences Institute of Physics <https://orcid.org/0000-0002-8086-0910>

Research Article

Keywords: Magnetic anisotropy, Interfacial state, Easy magnetization axis, Spin reorientation

Posted Date: March 17th, 2021

DOI: <https://doi.org/10.21203/rs.3.rs-300901/v1>

License:   This work is licensed under a Creative Commons Attribution 4.0 International License.

[Read Full License](#)

Version of Record: A version of this preprint was published at Chinese Physics Letters on September 1st, 2021. See the published version at <https://doi.org/10.1088/0256-307X/38/8/087502>.

Magnetic anisotropy induced by orbital occupation states in $\text{La}_{0.67}\text{Sr}_{0.33}\text{MnO}_3$ film

Huaixiang Wang^{1,2}, Jinghua Song^{1,2}, Weipeng Wang¹, Yuansha Chen¹, Xi Shen^{1,*}, Yuan Yao¹, Junjie Li¹, Jirong Sun^{1,2}, Richeng Yu^{1,2,*}

¹ *Beijing National Laboratory of Condensed Matter Physics, Institute of Physics, Chinese Academy of Sciences, Beijing 100190, P. R. China*

² *School of Physics Sciences, University of Chinese Academy of Sciences, Beijing 100049, P. R. China*

*Address correspondence to E-mail: rcyu@iphy.ac.cn; xshen@iphy.ac.cn

Abstract

Interface engineering is an effective and feasible method to regulate the magnetic anisotropy of films by altering interfacial states between different films. Using the technique of pulsed laser deposition, we prepared $\text{La}_{0.67}\text{Sr}_{0.33}\text{MnO}_3$ (LSMO) and $\text{La}_{0.67}\text{Sr}_{0.33}\text{MnO}_3/\text{SrCoO}_{2.5}$ (LSMO/SCO) films on the (110)-oriented $\text{La}_{0.3}\text{Sr}_{0.7}\text{Al}_{0.65}\text{Ta}_{0.35}\text{O}_3$ substrates. By covering the SCO film above the LSMO film, we transformed the easy magnetization axis of LSMO from the [001] axis to the $[1\bar{1}0]$ axis in the film plane. Based on statistical analyses, we found that the corresponding Mn-Mn ionic distances are different in the two types of LSMO films, causing different distortions of Mn-O octahedron in the LSMO film. In addition, it also induces diverse electronic occupation states in Mn^{3+} ions. The e_g electron of Mn^{3+} occupies $3z^2-r^2$ and x^2-y^2 orbitals in the LSMO and LSMO/SCO, respectively. We conclude that the electronic spin reorientation leads to the transformation of the easy magnetization axis in the LSMO films.

Keywords: Magnetic anisotropy, Interfacial state, Easy magnetization axis, Spin reorientation

1 Introduction

Transition metal oxide (TMO) films, especially the oxides processed by the interface engineering [1-6], have attracted extensive attention in the past decades owing to their diverse properties, such as interface charge transfer [7], two-dimensional electron gas [8], and discrepancy from bulk materials. Among TMOs, manganates exhibit distinctive performances as a result of the novel magnetic and electronic structures induced by the strong correlation between electrons as well as competition among lattice, charge, spin and orbit degrees of freedom, for instance, metal-insulator transition [9], colossal magnetoresistance [10, 11], magnetocaloric effects [12], and magnetoelectric coupling multiferroic effect [13].

For an epitaxial film, interfaces [6], strain induced by a mismatch with the substrate [14], and restriction of dimension [15] may break the delicate balance among different interactions and result in exotic properties. A fundamental property of magnetic materials is magnetic anisotropy (MA). MA plays a crucial role in many physical phenomena, including magnetic skyrmions [16], the magnetocaloric effect [17], and Kondo effect [18]. There are three types of MA existing in magnetic materials. Magnetocrystalline anisotropy, magnetoelastic coupling anisotropy, and shape anisotropy. Magnetocrystalline anisotropy is independent of grain size and shape while shape anisotropy is the dominant form of anisotropy in small size specimen [19, 20].

$\text{La}_{0.67}\text{Sr}_{0.33}\text{MnO}_3$ (LSMO), as a perovskite-type magnetic material, is a promising candidate for spintronics [21-23] material because of its room Curie temperature and 100% spin polarization [9]. For epitaxial thin films, different interfacial couplings cause different MA behaviors [1, 24-26]. MA in LSMO has been proved to be closely related to the occupation state of Mn $3d$ -orbital electrons [27]. In general, the mismatch of lattice constant at interface distorts the MnO_6 octahedra of LSMO and controls the electronic occupation state of Mn ions. Revealing the mechanism of MA in the LSMO film will enrich the corresponding scientific understanding and pave the way to future material designs and device applications of spintronic materials. In this work, we found that LSMO and $\text{La}_{0.67}\text{Sr}_{0.33}\text{MnO}_3/\text{SrCoO}_{2.5}$ (LSMO/SCO) films epitaxially grown on (110)-oriented $\text{La}_{0.3}\text{Sr}_{0.7}\text{Al}_{0.65}\text{Ta}_{0.35}\text{O}_3$ (LSAT)

substrates exhibit different MA behaviors. By using an aberration corrected transmission electron microscope, we analyzed the microstructures of the two films at the atomic scale and investigated the reason for causing the different MA.

2 Experiments

The LSMO and LSMO/SCO films were grown epitaxially on (110)-oriented LSAT substrates by using the pulsed laser deposition (PLD) method with a KrF excimer laser ($\lambda = 248$ nm). The LSMO layer is deposited at a temperature of 730 °C in an oxygen pressure of 30 Pa accompanying a laser fluence of 1.6 J/cm². And the SCO layer is deposited at 700 °C in an oxygen pressure of 12 Pa accompanying a laser fluence of 1.1 J/cm². The film thickness is determined by the time of deposition. The magnetic measurements were carried out in a Quantum Design vibrating sample magnetometer superconducting quantum interference device (VSM SQUID). The details of the fabrication and properties of the films can be found in Ref. [28].

Thin specimens for transmission electron microscopy (TEM) were prepared by mechanical polishing accompanied by Ar ion milling at liquid nitrogen temperature or focused ion beam (Helios 600I, FEI) technique. The selected area electron diffraction (SAED) observations were performed on a transmission electron microscope (CM200, Philips) with a field-emission gun (FEG) at 200kV. The high-angle annular dark-field (HAADF) images and electron energy loss spectroscopy (EELS) spectra were acquired on a scanning transmission electron microscope (STEM) equipped with double Cs correctors (CEOS) for the condenser lens and objective lens (ARM200F, JEOL) and a cold FEG at 200kV. Double tile holders were adopted in TEM studies and controlled by a TEM operate system to ensure the zone axis parallel to the electron beam in all TEM experiments.

3 Results and discussion

Two types of films were grown epitaxially on the (110)-oriented LSAT substrates, as shown schematically in Figs. 1c and d. Fig. 1c indicates a single layer LSMO film with a thickness of 6.5 nm and Fig. 1d is a bilayer film with 6.5 nm LSMO and 40 nm SCO. The

magnetizations of the two samples in a field cooling with $H=100\text{Oe}$ as a function of temperature are shown in Figs. 1a and b, respectively. The direction of the applied magnetic field is along the $[001]$ and $[1\bar{1}0]$ axes, respectively. The corresponding magnetizations are represented by pink and blue curves, respectively. In Figs. 1a and b, an obvious increase occurs around 300K, indicating a ferromagnetic transition. It should be noted that the magnetization along the $[001]$ axis is higher than that along the $[1\bar{1}0]$ axis below 280K in single layer film (SLF) [Fig. 1a], however, that is inverse in bilayer film (BLF) [Fig. 1b]. This means that the easy magnetization axis is along the $[001]$ direction in the SLF whereas along the $[1\bar{1}0]$ direction in the BLF.

It is well known that LSAT is a diamagnetic material with a perovskite structure (space group of $Pm-3m$) [29, 30] and SCO has a G -type antiferromagnetic orthorhombic structure with a space group of $Ima2$ [31]. Therefore, the ferromagnetism only originates from the LSMO film. Meanwhile, there is an extraordinarily strong double exchange interaction between Mn^{3+} and Mn^{4+} ions in the LSMO below T_C [32]. Because of the effect of the crystal field in the LSMO, d -orbitals of Mn ion will split into e_g and t_{2g} orbitals [33]. Moreover, the Jahn-Teller effect [34] degenerates e_g orbitals into x^2-y^2 and $3z^2-r^2$ orbitals. The electronic occupation state of Mn ions is closely related to the crystal structure of LSMO.

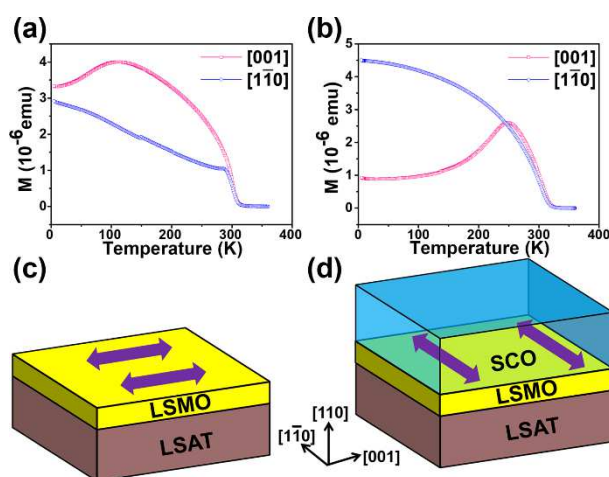


Fig. 1 a and b Magnetizations as a function of temperature in a field cooling with $H=100\text{Oe}$ corresponding to the LSMO and LSMO/SCO films, respectively. c and d Schematic diagrams of LSMO and LSMO/SCO films (purple arrows represent the easy magnetization axes)

In order to explore the microstructures and transformation of the easy magnetization axis in the LSMO film, we carried out TEM observations for the film samples along the cross-section direction at the atomic scale. Fig. 2 shows HAADF STEM images of the two samples, indicating the thickness of 6.5 nm for the LSMO and a sharp boundary between the LSMO and LSAT. A bulk LSMO has a pseudo-cubic structure with $R-3c$ space group [35]. When it is grown epitaxially on a cubic structure substrate, it will retain the pseudo-cubic structure. Thus, grown on LSAT, the LSMO film exhibits a perovskite structure, as shown in Figs. 2a and b. Since the contrast intensity is approximately proportional to Z^2 (Z is the atomic number) in HAADF STEM images [36], the brightest spots in the LSMO layer in HAADF images represent La(Sr) atomic columns, and the fainter spots correspond to Mn atomic columns. The O atoms could not be observed in the HAADF image since their scattering is too weak to be acquired at acceptance angles of 90-370 mrad (HAADF). However, there is an indistinct borderline between the LSMO and SCO layers, which instructs a mixed trace of the two components closing to the interface. Besides, parallel dark stripes occur in the SCO layer and have an angle of 45° relative to the interface, as shown in Fig. 2d. These dark stripes indicate that the SCO film has a typical brownmillerite structure [37, 38] rather than a perovskite structure.

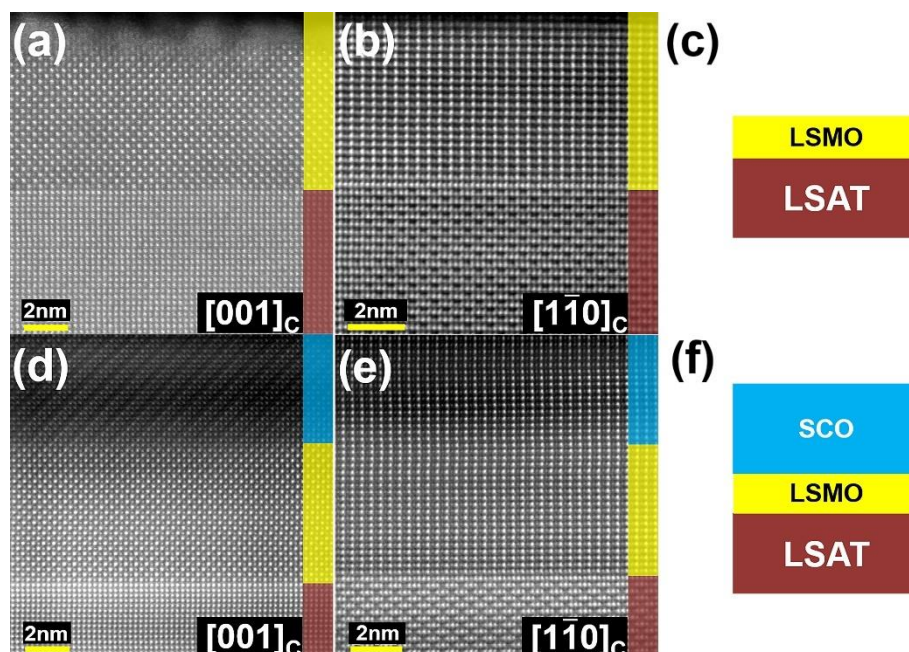


Fig. 2 a and b Cross-sectional HAADF images of LSMO SLF along the $[001]$ and $[1\bar{1}0]$ axes, respectively. **d and e** Cross-sectional HAADF images of LSMO BLF along the $[001]$ and $[1\bar{1}0]$ axes, respectively. **c and f** Schematic diagrams of SLF and BLF, respectively (subscript “C” in the HAADF images indicates cubic structure)

Figs. 3a-d are the corresponding SAED patterns. All diffraction spots in Figs. 3a and b confirm that the LSMO has the same structure as the LSAT. Compared to Figs. 3a and b, Figs. 3c and d show additional spots (marked by red arrows) from the SCO film. In Fig. 3b, the spots rounded by the yellow dotted circles represent an ordered structure in the LSAT [see Figs. 2b and e]. Al and Ta atoms are locally orderly arranged in B-site of perovskite, which induces a face-centered-cubic structure with double of the original cell parameters [39].

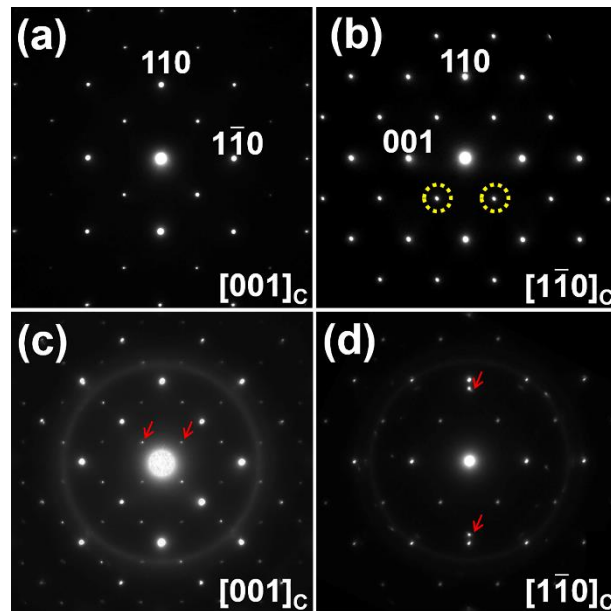


Fig. 3 a and b Cross-sectional SAED patterns of SLF corresponding to Figs. 2a and b. **c and d** Cross-sectional patterns of BLF corresponding to Figs. 2d and e (spots marked by red arrows come from the SCO film)

Particularly, in order to research the 45° dark stripes in the SCO layer, the HAADF image closing to the interface between the SCO and LSMO along the $[001]$ zone axis is shown in Fig. 4a, where the SCO grows to form 90° domains (yellow arrows indicate dark stripes). Such domain structures are also confirmed by the diffraction spots marked by red arrows in Fig. 3c. Fig. 4b is a magnified figure of the dotted line rectangle part in Fig. 4a, which matches well with the structural model of SCO in Fig. 4c. CoO_6 octahedra and CoO_4

tetrahedra arrange alternately along the $[100]_c$ and $[010]_c$ directions, as shown in Figs. 4b and c. The dark stripes in HAADF images are corresponding to the CoO_4 tetrahedra, indicating a larger Sr-Sr atomic distance compared to that of CoO_6 octahedra in bright stripes. Thus, we deduce that a perovskite-brownmillerite interface plays a significant role in the MA in LSMO [2, 40].

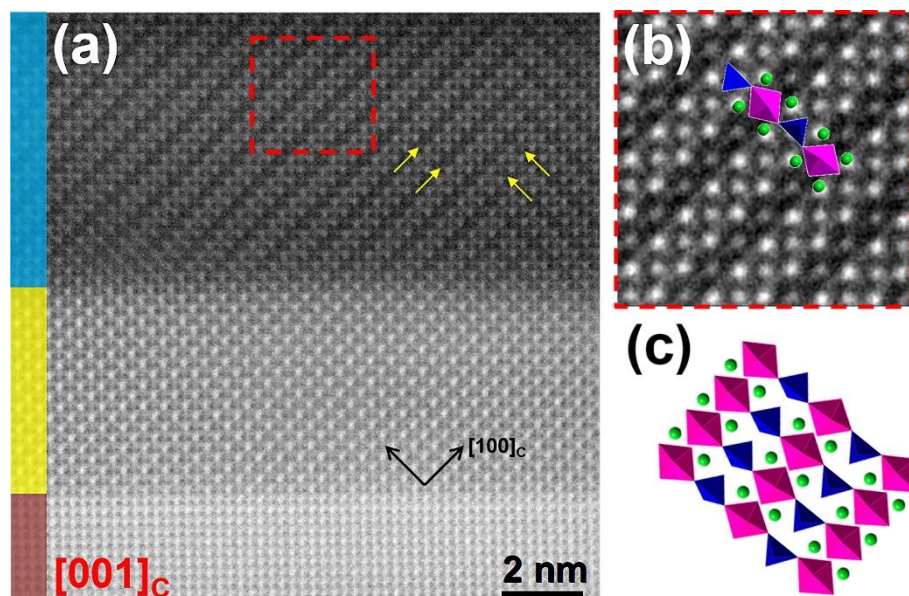


Fig. 4 a The HAADF image of cross-sectional LSMO BLF along the $[001]$ zone axis. Yellow arrows indicate dark stripes in the SCO layer. **b** The magnified image of the dotted line rectangle part in **a** and a corresponding structural model overlapped with it. **c** The structural model of SCO (The purple and blue polyhedral represent Co-O octahedra and Co-O tetrahedra, and green balls represent Sr atoms)

Furthermore, in order to quantitatively study the structural difference of LSMO between SLF and BLF, we carried out statistical analyses for the distances of adjacent Mn atoms in corresponding HAADF images. As presented in Fig. 5, we compare the Mn-Mn interatomic distances along the $[001]$, $[1\bar{1}0]$ and $[110]$ directions, which are named as $\zeta_{[001]}$, $\zeta_{[1\bar{1}0]}$ and $\zeta_{[110]}$, respectively. The relationship between the distance and Mn-O octahedron is presented in Fig. 5e. Figs. 5a and b show the comparisons between $\zeta_{[1\bar{1}0]}$ and $\zeta_{[110]}$ averaged from the HAADF image along the $[001]$ zone axis and between $\zeta_{[001]}$ and $\zeta_{[110]}$ averaged from the HAADF image along the $[1\bar{1}0]$ zone axis in SLF, respectively. Figs. 5c and d show the same comparisons in BLF. Each data point was averaged by dozens of Mn-Mn interatomic

distances in corresponding lines. The dotted lines are the averaged values of the corresponding data.

Because $\zeta_{[001]}$ and $\zeta_{[1\bar{1}0]}$ were got from different HAADF images, we choose $\zeta_{[110]}$ as a reference to compare $\zeta_{[001]}$ and $\zeta_{[1\bar{1}0]}$.

In SLF:

$$\zeta_{[1\bar{1}0]} / \zeta_{[110]} = 97.41\%$$

$$\zeta_{[001]} / \zeta_{[110]} = 99.66\%$$

thus, we obtain: $\zeta_{[001]} > \zeta_{[1\bar{1}0]}$

In BLF:

$$\zeta_{[1\bar{1}0]} / \zeta_{[110]} = 99.19\%$$

$$\zeta_{[001]} / \zeta_{[110]} = 98.73\%$$

thus, we obtain: $\zeta_{[001]} < \zeta_{[1\bar{1}0]}$

As we mentioned above, crystal distortion of perovskite degenerates e_g orbitals into x^2-y^2 and $3z^2-r^2$ orbitals. The magnetic moment of LSMO mainly comes from the spin moment of Mn ions, but the direction of the magnetic moment is affected by the occupied orbital direction. In SLF, $\zeta_{[001]} > \zeta_{[1\bar{1}0]}$ causes an elongated octahedral along the [001] direction, as shown in Fig. 5f, and the lower energy of $3z^2-r^2$ orbital compared to x^2-y^2 orbital. In this case, the e_g electron of Mn^{3+} preferentially occupies $3z^2-r^2$ orbital. According to Bruno model [24], this induces an easy magnetization axis along the [001] direction. Relatively, in BLF, $\zeta_{[001]} < \zeta_{[1\bar{1}0]}$ leads to a compressed octahedral along the [001] direction, as shown in Fig. 5f, and the lower energy of x^2-y^2 orbital, thus, the e_g electron prefers to occupy x^2-y^2 orbital. In the LSMO film plane, the $[1\bar{1}0]$ direction is along the projection of the x^2-y^2 orbital. So, the occupation of e_g electron in x^2-y^2 orbital induces an easy magnetization axis along the $[1\bar{1}0]$ direction. This is consistent with the result of x-ray linear dichroism [28].

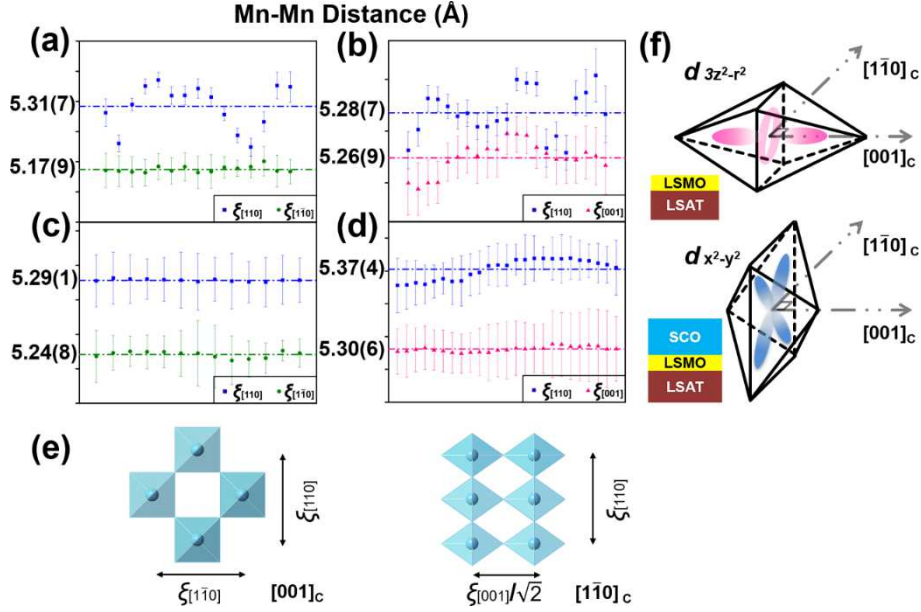


Fig. 5 The statistical interatomic distances of Mn-Mn. **a** $\zeta_{[1\bar{1}0]}$ and $\zeta_{[110]}$ in SLF obtained from the HAADF image along the $[001]_c$ zone axis. **b** $\zeta_{[001]}$ and $\zeta_{[110]}$ in SLF obtained from the HAADF image along the $[1\bar{1}0]_c$ zone axis. **c** $\zeta_{[1\bar{1}0]}$ and $\zeta_{[110]}$ in BLF obtained from the HAADF image along the $[001]_c$ zone axis. **d** $\zeta_{[001]}$ and $\zeta_{[110]}$ in BLF obtained from the HAADF image along the $[1\bar{1}0]_c$ zone axis. Each data point is averaged by the Mn-Mn distances along a row or a column. The dotted lines are the average values of all corresponding data. **e** Schematic Mn-Mn distances of $\zeta_{[001]}$, $\zeta_{[1\bar{1}0]}$ and $\zeta_{[110]}$ in the structure. **f** The elongated and compressed Mn-O octahedral of LSMO along the $[001]_c$ direction

Charge transfer between Mn and Co ions was mentioned to explain the phenomenon of MA in an LSMO film [40]. In Fig. 6, we present the EELS spectra of the BLF film in an energy range from 625 eV to 875 eV. Each spectrum is an integration of the line scan profiles along the $[1\bar{1}0]$ direction when the sample was observed along the $[001]$ zone axis. We obtained EELS spectra from the LSMO layer to the SCO layer across the interface as shown in Fig. 6. Obviously, near the interface between LSMO and SCO, both of the Mn and Co peaks appear simultaneously, indicating a mixture of several atomic layers. This is consistent with the blurry borderline in Fig. 2d and causes stronger crystal distortions. However, there is no obvious shift of Mn L edge from the LSMO layer to the interface, indicating no change of valence state for Mn ions. On the contrary, a shift of the Co L_3 peak toward low energy can be noticed from the Co layer to the interface, suggesting a decrease of valence state for Co ions. This may be caused by the existence of $\text{SrCoO}_{3-\delta}$ ($0 < \delta < 1$) in local areas as an impurity

in SrCoO_{2.5} film [28, 41]. Therefore, there may be no charge transfer between Mn and Co ions in the BLF.

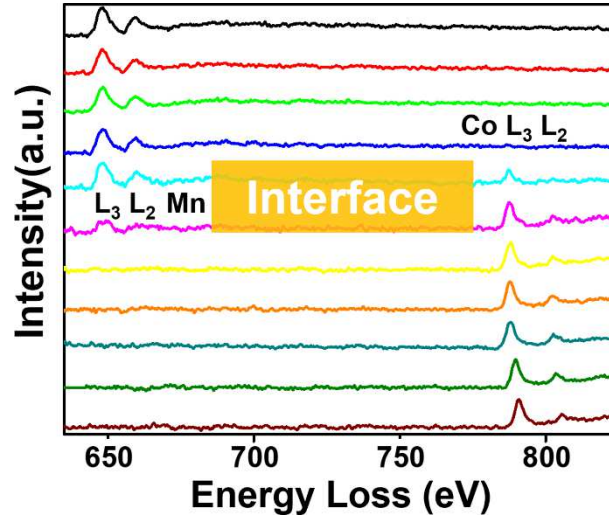


Fig. 6 Integrated EELS spectra from the LSMO layer to the SCO layer

4 Conclusions

We investigated the MA of LSMO film in LSMO and LSMO/SCO films grown epitaxially on (100)-oriented LSAT substrates. Magnetic measurements display an easy magnetization axis of LSMO along the [001] direction in SLF while along the [1 $\bar{1}$ 0] direction in BLF. Through the quantitative statistical analyses, we found that the Mn-O octahedral distortions are different in these two film samples. In SLF, the octahedra are elongated, while in BLF, the octahedra are compressed. This gives rise to the preferential occupation of e_g electron in the $3z^2-r^2$ orbital of Mn in SLF while in the x^2-y^2 orbital in BLF. Thus, it is concluded that the anomalous MA transformation of LSMO from the [001] direction in SLF to the [1 $\bar{1}$ 0] in BLF originates from a spin orientation of Mn ions. Our EELS spectra reveal that there is no detectable charge transfer between Mn and Co ions.

Acknowledgements

This work was supported by the National Key Research Program of China (Grant Nos. 2017YFA0206200, 2016YFA0300701 and 2018YFA0208402), the National Natural Science Foundation of China (Grant Nos. 11934017, 11874413, 11574376 and 51972333) and the

Strategic Priority Research Program of the Chinese Academy of Sciences, No. XDB33030200. One of the authors, X. Shen, was sponsored by the Youth Innovation Promotion Association of CAS (2019009).

Declarations

Funding

The National Key Research Program of China (Grant Nos. 2017YFA0206200, 2016YFA0300701 and 2018YFA0208402); the National Natural Science Foundation of China (Grant Nos. 11934017, 11874413, 11574376 and 51972333); the Strategic Priority Research Program of the Chinese Academy of Sciences, No. XDB33030200 and the Youth Innovation Promotion Association of CAS (2019009).

Conflicts of interest

The authors declare that they have no known competing financial interests or personal relationships that could have appeared to influence the work reported in this paper.

Availability of data and material

The datasets used or analyzed during the current study are available from the corresponding author on reasonable request.

Code availability

Not applicable.

Authors' contributions

Not applicable.

Ethics approval

Not applicable.

Consent to participate

Not applicable.

Consent for publication

Not applicable.

References

- [1] D. Yi, J. Liu, S.-L. Hsu, L. Zhang, Y. Choi, J.-W. Kim, Z. Chen, J. D. Clarkson, C. R. Serrao, E. Arenholz, P. J. Ryan, H. Xu, R. J. Birgeneau, R. Ramesh, Proc. Natl. Acad. Sci. USA **113**, 6397 (2016)
<https://doi.org/10.1073/pnas.1524689113>.
- [2] J. Zhang, Z. Zhong, X. Guan, X. Shen, J. Zhang, F. Han, H. Zhang, H. Zhang, X. Yan, Q. Zhang, L. Gu, F. Hu, R. Yu, B. Shen, J. Sun, Nat. Commun. **9**, 1923 (2018)
<https://doi.org/10.1038/s41467-018-04304-7>.
- [3] J. Song, Y. Chen, H. Zhang, F. Han, J. Zhang, X. Chen, H. Huang, J. Zhang, H. Zhang, X. Yan, T. Khan, S. Qi, Z. Yang, F. Hu, B. Shen, J. Sun, Phys. Rev. Mater. **3**, 045801 (2019)
<https://doi.org/10.1103/PhysRevMaterials.3.045801>.
- [4] X. Guan, X. Shen, J. Zhang, W. Wang, J. Zhang, H. Wang, W. Wang, Y. Yao, J. Li, C. Gu, J. Sun, R. Yu, Phys. Rev. B **100**, 014427 (2019)
<https://doi.org/10.1103/PhysRevB.100.014427>.
- [5] E. Dagotto, Science **318**, 1076 (2007)
<https://doi.org/10.1126/science.1151094>.
- [6] H. Y. Hwang, Y. Iwasa, M. Kawasaki, B. Keimer, N. Nagaosa, Y. Tokura, Nat. Mater. **11**, 103 (2012)
<https://doi.org/10.1038/nmat3223>.
- [7] J. Chakhalian, J. W. Freeland, H.-U. Habermeier, G. Cristiani, G. Khaliullin, M. van Veenendaal, B. Keimer, Science **318**, 1114 (2007)
<https://doi.org/10.1126/science.1149338>.
- [8] A. Ohtomo, H. Y. Hwang, Nature **427**, 423 (2004)
<https://doi.org/10.1038/nature02308>.
- [9] J.-H. Park, E. Vescovo, H.-J. Kim, C. Kwon, R. Ramesh, T. Venkatesan, Nature **392**, 794 (1998)
<https://doi.org/10.1038/33883>.
- [10] S. Jin, T. H. Tiefel, M. McCormack, R. A. Fastnacht, R. Ramesh, L. H. Chen, Science **264**, 413 (1994)
<https://doi.org/10.1126/science.264.5157.413>.

- [11] R. von Helmolt, J. Wecker, B. Holzapfel, L. Schultz, K. Samwer, *Phys. Rev. Lett.* **71**, 2331 (1993)
<https://doi.org/10.1103/PhysRevLett.71.2331>.
- [12] X. Moya, L. E. Hueso, F. Maccherozzi, A. I. Tovstolytkin, D. I. Podyalovskii, C. Ducati, L. C. Phillips, M. Ghidini, O. Hovorka, A. Berger, M. E. Vickers, E. Defay, S. S. Dhesi, N. D. Mathur, *Nat. Mater.* **12**, 52 (2013)
<https://doi.org/10.1038/nmat3463>
- [13] T. Kimura, T. Goto, H. Shintani, K. Ishizaka, T. Arima, Y. Tokura, *Nature* **426**, 55 (2003)
<https://doi.org/10.1038/nature02018>.
- [14] J. Cao, J. Wu, *Mater. Sci. Eng. R Rep.* **71**, 35 (2011)
<https://doi.org/10.1016/j.mser.2010.08.001>.
- [15] A. V. Boris, Y. Matiks, E. Benckiser, A. Frano, P. Popovich, V. Hinkov, P. Wochner, M. Castro-Colin, E. Detemple, V. K. Malik, C. Bernhard, T. Prokscha, A. Suter, Z. Salman, E. Morenzoni, G. Cristiani, H.-U. Habermeier, B. Keimer, *Science* **332**, 937 (2011)
<https://doi.org/10.1126/science.1202647>.
- [16] U. K. Rößler, A. N. Bogdanov, C. Pfleiderer, *Nature* **442**, 797 (2006)
<https://doi.org/10.1038/nature05056>.
- [17] M. S. Reis, R. M. Rubinger, N. A. Sobolev, M. A. Valente, K. Yamada, K. Sato, Y. Todate, A. Bouravleuv, P. J. von Ranke, S. Gama, *Phys. Rev. B* **77**, 104439 (2008)
<https://doi.org/10.1103/PhysRevB.77.104439>.
- [18] A. F. Otte, M. Ternes, K. von Bergmann, S. Loth, H. Brune, C. P. Lutz, C. F. Hirjibehedin, A. J. Heinrich, *Nat. Phys.* **4**, 847 (2008)
<https://doi.org/10.1038/nphys1072>.
- [19] P. Pouloupoulos, K. Baberschke, *J. Phys.: Condens. Matter* **11**, 9495 (1999)
<https://doi.org/10.1088/0953-8984/11/48/310>.
- [20] R. Allenspach, *J. Magn. Magn. Mater.* **129**, 160 (1994)
[https://doi.org/10.1016/0304-8853\(94\)90108-2](https://doi.org/10.1016/0304-8853(94)90108-2).
- [21] A. Fert, A. Barthélémy, J. B. Youssef, J.-P. Contour, V. Cros, J. M. De Teresa, A. Hamzic, J. M. George, G. Faini, J. Grollier, H. Jaffrès, H. Le Gall, F. Montaigne, F. Pailloux, F. Petroff, *Mater. Sci. Eng. B* **84**, 1 (2001)

[https://doi.org/10.1016/S0921-5107\(01\)00548-7](https://doi.org/10.1016/S0921-5107(01)00548-7).

[22] V. Garcia, M. Bibes, L. Bocher, S. Valencia, F. Kronast, A. Crassous, X. Moya, S. Enouz-Vedrenne, A. Gloter, D. Imhoff, C. Deranlot, N. D. Mathur, S. Fusil, K. Bouzehouane, A. Barthelemy, *Science* **327**, 1106 (2010)

<https://doi.org/10.1126/science.1184028>.

[23] D. Pantel, S. Goetze, D. Hesse, M. Alexe, *Nat. Mater.* **11**, 289 (2012)

<https://doi.org/10.1038/nmat3254>.

[24] J. Zhang, X. Yan, F. Han, J. Zhang, D. Liu, B. Shen, J. Sun, *AIP Adv.* **8**, 055809 (2018)

<https://doi.org/10.1063/1.5007169>.

[25] Y. Okada, D. Walkup, H. Lin, C. Dhital, T.-R. Chang, S. Khadka, W. Zhou, H.-T. Jeng, M. Paranjape, A. Bansil, Z. Wang, S. D. Wilson, V. Madhavan, *Nat. Mater.* **12**, 707 (2013)

<https://doi.org/10.1038/nmat3653>.

[26] S. Majumdar, K. Kooser, T. Elovaara, H. Huhtinen, S. Granroth, P. Paturi, *J. Phys.: Condens. Matter* **25**, 376003 (2013)

<https://doi.org/10.1088/0953-8984/25/37/376003>.

[27] P. Bruno, *Phys. Rev. B* **39**, 865 (1989)

<https://doi.org/10.1103/PhysRevB.39.865>.

[28] J. Song, Y. Chen, X. Chen, H. Wang, T. Khan, F. Han, J. Zhang, H. Huang, J. Zhang, H. Zhang, H. Zhang, X. Yan, S. Qi, F. Hu, B. Shen, R. Yu, J. Sun, *Phys. Rev. Appl.* **12**, 054016 (2019)

<https://doi.org/10.1103/PhysRevApplied.12.054016>.

[29] M. Khalid, A. Setzer, M. Ziese, P. Esquinazi, D. Spemann, A. Pöppel, E. Goering, *Phys. Rev. B* **81**, 214414 (2010)

<https://doi.org/10.1103/PhysRevB.81.214414>.

[30] D. Y. Wang, J. Wang, H. L. W. Chan, and C. L. Choy, *J. Appl. Phys.* **101**, 043515 (2007)

<https://doi.org/10.1063/1.2646014>.

[31] A. Muñoz, C. de la Calle, J. A. Alonso, P. M. Botta, V. Pardo, D. Baldomir, J. Rivas, *Phys. Rev. B* **78**, 054404 (2008)

<https://doi.org/10.1103/PhysRevB.78.054404>.

[32] P. W. Anderson and H. Hasegawa, *Phys. Rev.* **100**, 675 (1955)

<https://doi.org/10.1103/PhysRev.100.675>.

[33] Y. Tokura, Science **288**, 462 (2000)

<https://doi.org/10.1126/science.288.5465.462>.

[34] H. Jahn, E. Teller, Proc. R. Soc. Lond. A **161**, 220 (1937)

<https://doi.org/10.1098/rspa.1937.0142>

[35] G. Venkataiah, D. C. Krishna, M. Vithal, S. S. Rao, S. V. Bhat, V. Prasad, S. V. Subramanyam, P. V. Reddy, Physica B: Condens. Matter **357**, 370 (2005)

<https://doi.org/10.1016/j.physb.2004.12.001>.

[36] D. E. Jesson, S. J, Proc. R. Soc. Lond. A **449**, 273 (1995)

<https://doi.org/10.1098/rspa.1995.0044>

[37] J. Zhang, X. Chen, Q. Zhang, F. Han, J. Zhang, H. Zhang, H. Zhang, H. Huang, S. Qi, X. Yan, L. Gu, Y. Chen, F. Hu, S. Yan, B. Liu, B. Shen, J. Sun, ACS Appl. Mater. Interfaces **10**, 40951 (2018)

<https://doi.org/10.1021/acsami.8b14981>.

[38] W. Wang, J. Zhang, X. Shen, X. Guan, Y. Yao, J. Li, C. Gu, J. Sun, Y. Zhu, J. Tao, R. Yu, Phys. Rev. B **101**, 024406 (2020)

<https://doi.org/10.1103/PhysRevB.101.024406>.

[39] H. Li, L. Salamanca-Riba, R. Ramesh, J. H. Scott, J. Mater. Res. **18**, 1698 (2003)

<https://doi.org/10.1557/JMR.2003.0233>.

[40] B. Cui, F. Li, C. Song, J. Peng, M. S. Saleem, Y. Gu, S. Li, K. Wang, F. Pan, Phys. Rev. B **94**, 134403 (2016)

<https://doi.org/10.1103/PhysRevB.94.134403>.

[41] Q. Zhang, X. He, J. Shi, N. Lu, H. Li, Q. Yu, Z. Zhang, L. Chen. B. Morris, Q. Xu, P. Yu, L. Gu, K. Jin, C. Nan, Nat. Commun. **8**, 104 (2017)

<https://doi.org/10.1038/s41467-017-00121-6>.

Figures

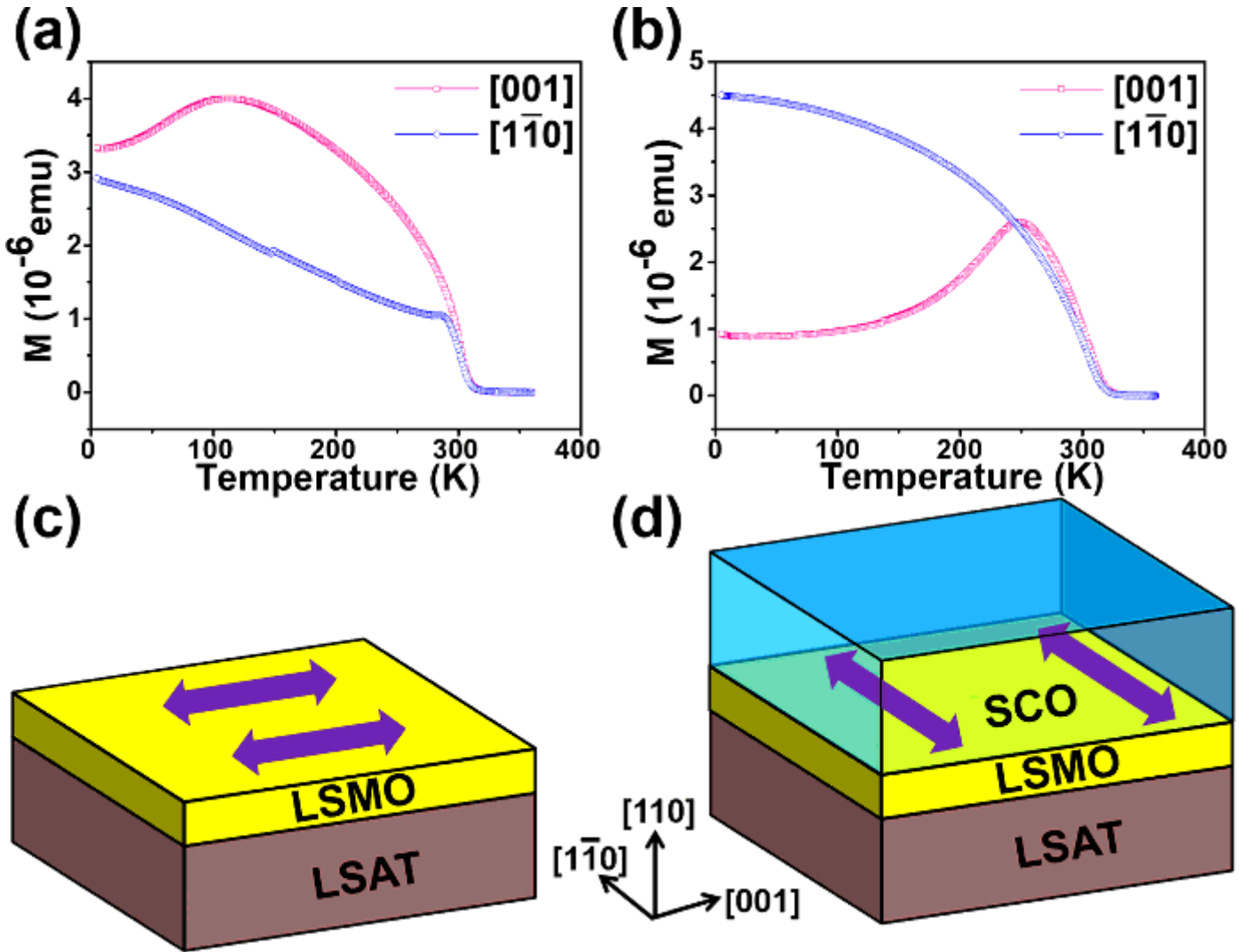


Figure 1

a and b Magnetizations as a function of temperature in a field cooling with $H=1000$ e corresponding to the LSMO and LSMO/SCO films, respectively. c and d Schematic diagrams of LSMO and LSMO/SCO films (purple arrows represent the easy magnetization axes)

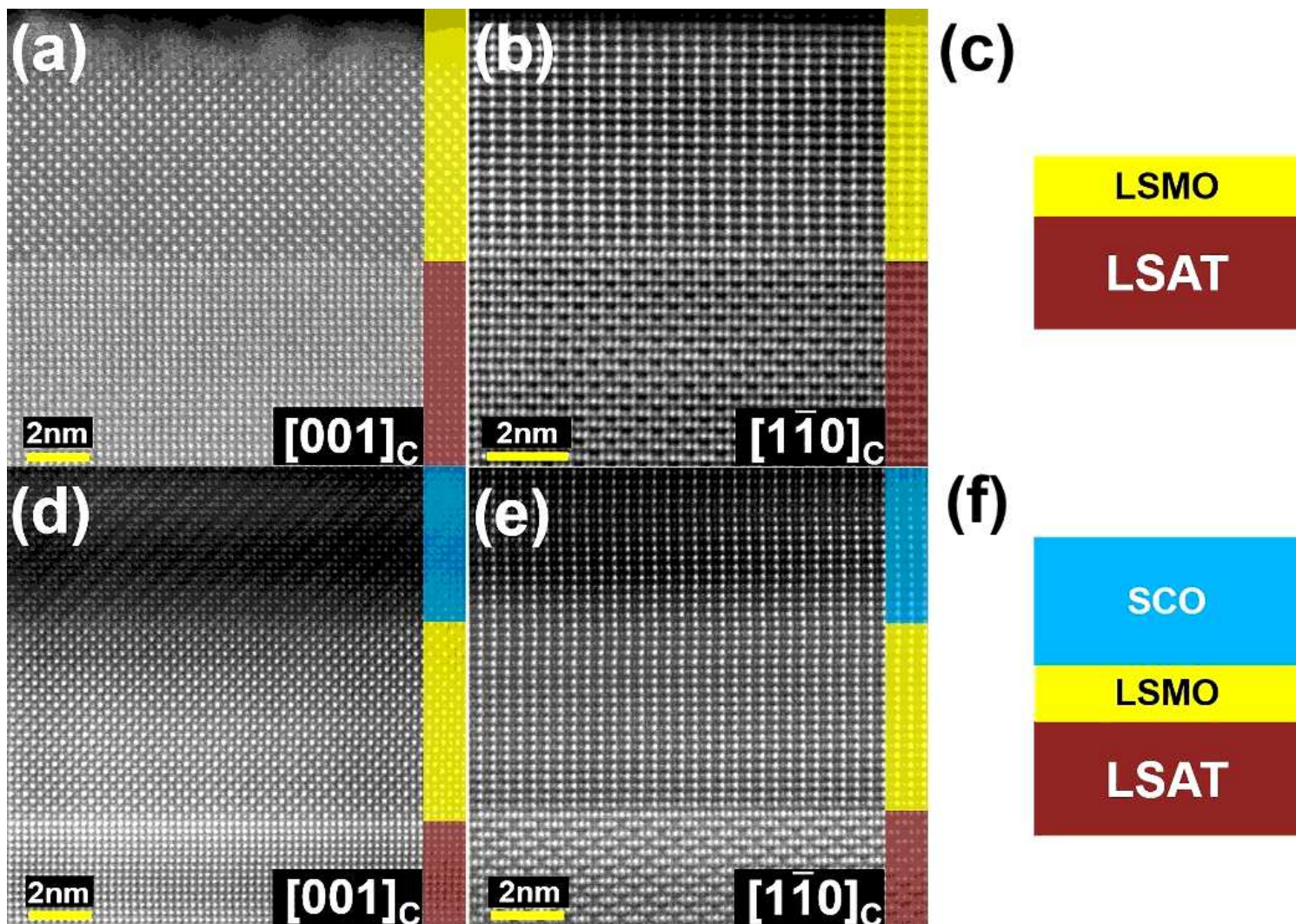


Figure 2

Please see the Manuscript PDF file for the complete figure caption

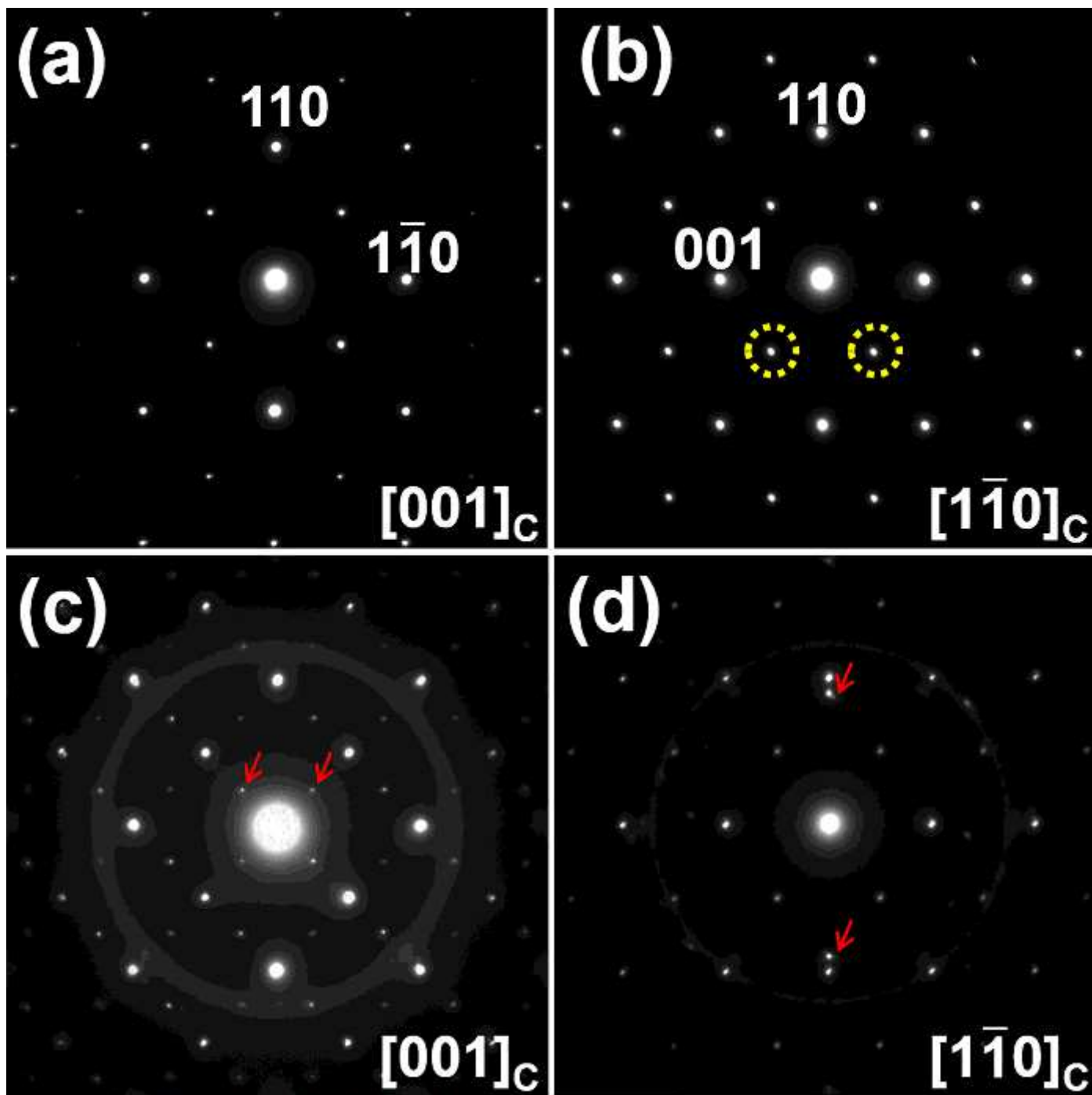


Figure 3

a and b Cross-sectional SAED patterns of SLF corresponding to Figs. 2a and b. c and d Cross-sectional patterns of BLF corresponding to Figs. 2d and e (spots marked by red arrows come from the SCO film)

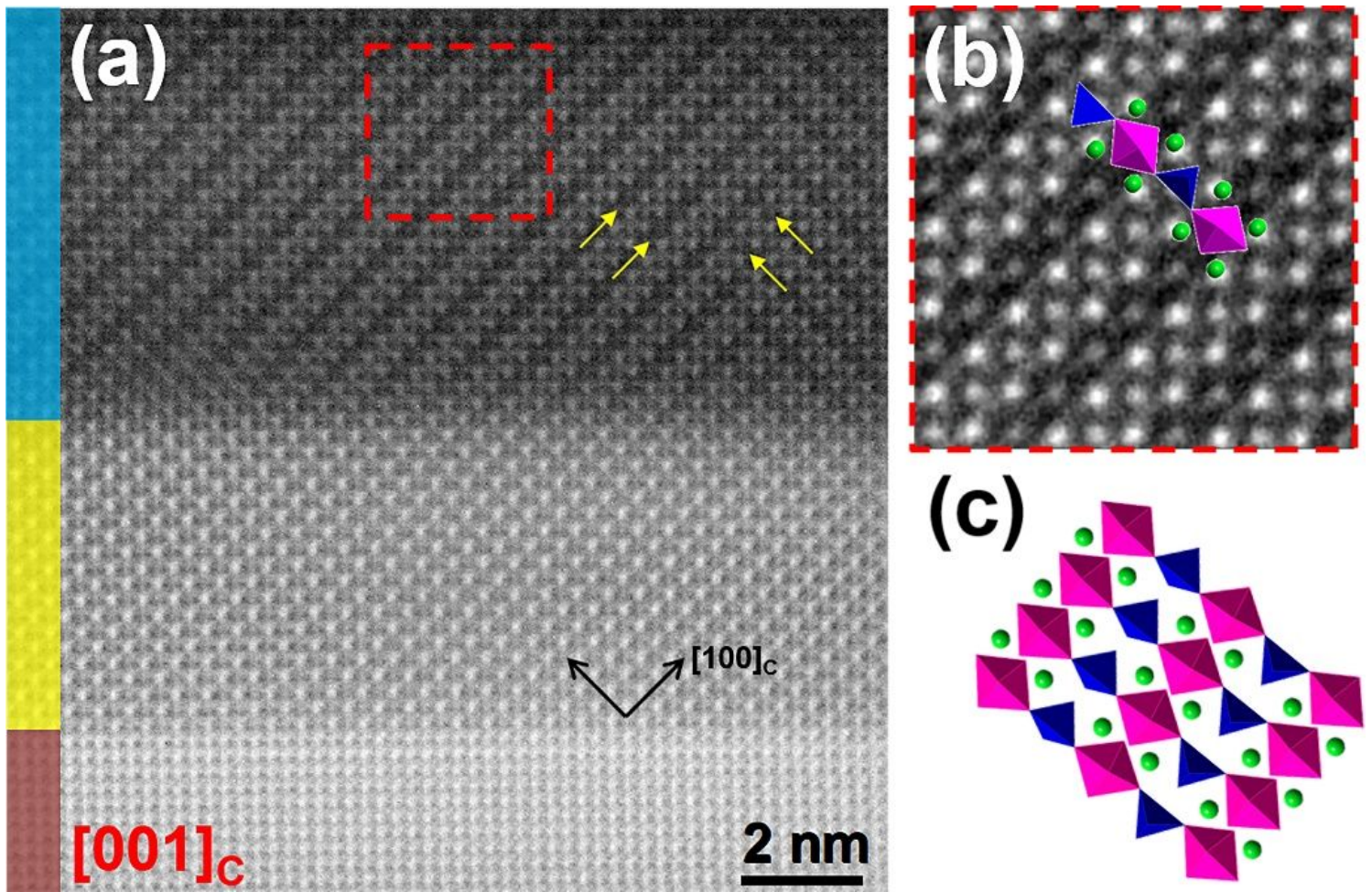


Figure 4

a The HAADF image of cross-sectional LSMO BLF along the $[001]$ zone axis. Yellow arrows indicate dark stripes in the SCO layer. b The magnified image of the dotted line rectangle part in a and a corresponding structural model overlapped with it. c The structural model of SCO (The purple and blue polyhedral represent Co-O octahedra and Co-O tetrahedra, and green balls represent Sr atoms)

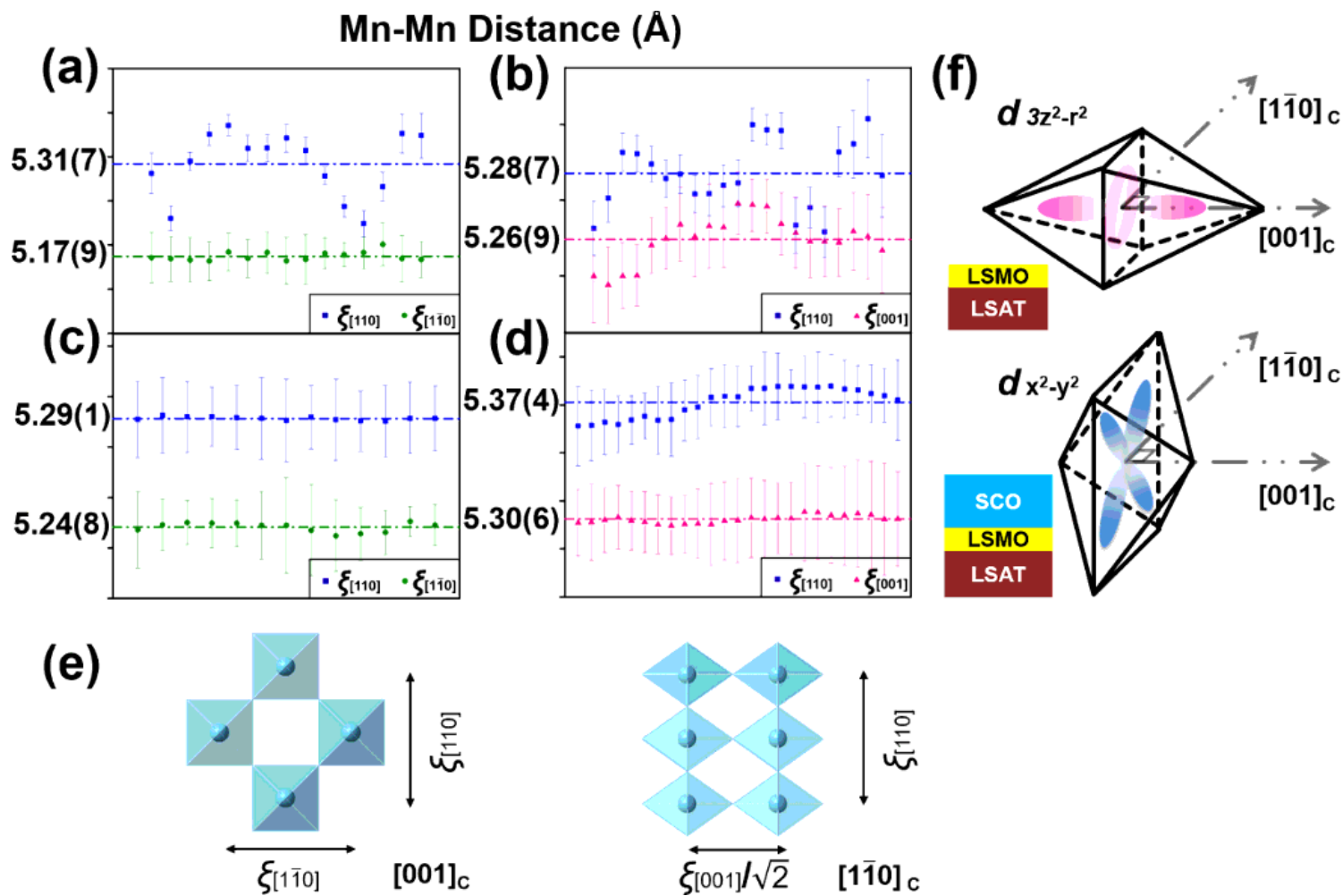


Figure 5

Please see the Manuscript PDF file for the complete figure caption

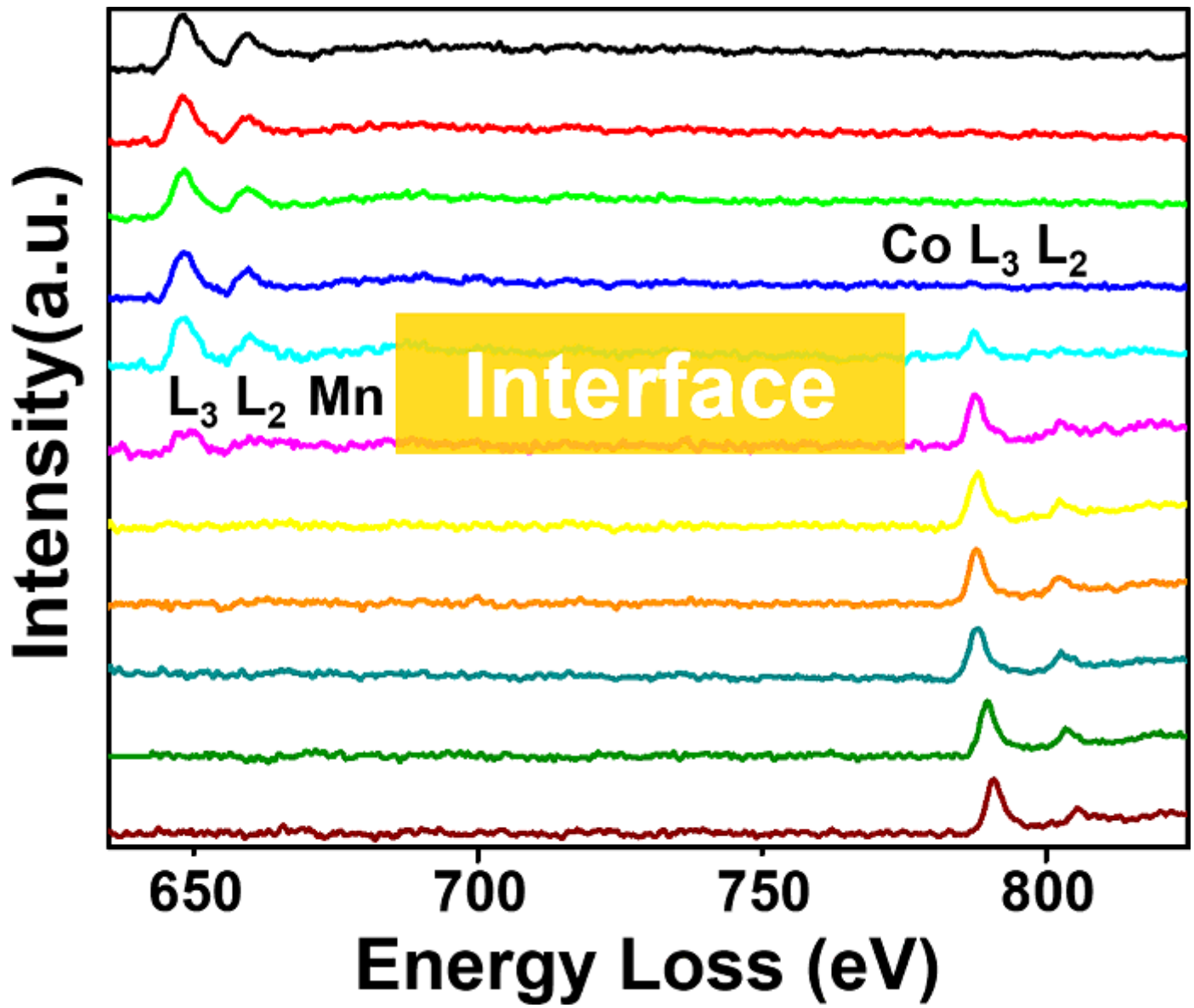


Figure 6

Integrated EELS spectra from the LSMO layer to the SCO layer